Tuning the circularly polarized luminescence in homoleptic and heteroleptic chiral Cr^{III} complexes

Poncet, Maxime Arnaud; Besnard, Céline; Guenee, Laure; Jimenez, Juan; Piguet, Claude

How to cite

PONCET, Maxime Arnaud et al. Tuning the circularly polarized luminescence in homoleptic and heteroleptic chiral Cr^{III} complexes. In: Frontiers in chemistry, 2024, vol. 12, p. 1472943. doi: 10.3389/fchem.2024.1472943

This publication URL: https://archive-ouverte.unige.ch/unige:180731

Publication DOI: 10.3389/fchem.2024.1472943

frontiers | Frontiers in Chemistry

TYPE Original Research
PUBLISHED 09 October 2024
DOI 10.3389/fchem.2024.1472943

OPEN ACCESS

EDITED BY
Fabio Piccinelli,
University of Verona, Italy

REVIEWED BY
Marco M. Allard,
La Sierra University, United States
Jatish Kumar,
Indian Institute of Science Education and Research, India
Yu-Wu Zhong,
Chinese Academy of Sciences (CAS), China

*CORRESPONDENCE
Claude Piguet,
claude.piguet@unige.ch
Juan-Ramón Jiménez,
jrjimenez@ugr.es

RECEIVED 30 July 2024
ACCEPTED 20 September 2024
PUBLISHED 09 October 2024

CITATION
Poncet M, Besnard C, Guénée L, Jiménez J-R and Piguet C (2024) Tuning the circularly polarized luminescence in homoleptic and heteroleptic chiral Cr^{III} complexes. *Front. Chem.* 12:1472943. doi: 10.3389/fchem.2024.1472943

Tuning the circularly polarized luminescence in homoleptic and heteroleptic chiral Cr^{III} complexes

Maxime Poncet[1], Céline Besnard[2], Laure Guénée[2], Juan-Ramón Jiménez[3]* and Claude Piguet[1]*

[1]Department of Inorganic and Analytical Chemistry, University of Geneva, Geneva, Switzerland, [2]Laboratory of Crystallography, University of Geneva, Geneva, Switzerland, [3]Department of Inorganic Chemistry, University of Granada, Unidad de Excelencia de Química (UEQ), Granada, Spain

A series of highly emissive inert and chiral Cr^{III} complexes displaying positive and negative circularly polarized luminescence (CPL) within the near-infrared (NIR) region at room temperature have been prepared and characterized to decipher the effect of ligand substitution on the photophysical properties, more specifically on the chiroptical properties. The helical homoleptic $[Cr(dqp\text{-}R)_2]^{3+}$ (dqp = 2,6-di(quinolin-8-yl)pyridine; R = Ph, ≡-Ph, DMA, ≡-DMA (DMA = *N*,*N*-dimethylaniline)) and heteroleptic $[Cr(dqp)(L)]^{3+}$ (L = 4-methoxy-2,6-di(quinolin-8-yl)pyridine (dqp-OMe) or L = N^2,N^6-dimethyl-N^2,N^6-di(pyridin-2-yl)pyridine-2,6-diamine (ddpd)) molecular rubies were synthesized as racemic mixtures and then resolved and isolated into their respective pure *PP* and *MM* enantiomeric forms by chiral stationary phase HPLC. The corresponding enantiomers show two opposite polarized emission bands within the 700–780 nm range corresponding to the characteristic metal-centered $Cr(^2E' \rightarrow {}^4A_2)$ and $Cr(^2T_1' \rightarrow {}^4A_2)$ transitions with large g_{lum} ranging from 0.14 to 0.20 for the former transition. In summary, this study reports the rational use of different ligands on Cr^{III} and their effect on the chiroptical properties of the complexes.

KEYWORDS

chromium, chirality, emission, circularly polarized luminescence, circular dichroism, chiral HPLC

1 Introduction

Chiral chromophores displaying intense circularly polarized luminescence (CPL) signal and high CPL brightness (B_{CPL}) are up-and-coming candidates for applications as molecular probes in biological systems (Carr et al., 2012; Staszak et al., 2019), in bio-imaging (Heffern et al., 2014), in light-emitting devices (e.g., CP-OLEDs) (Brandt et al., 2017; Zinna et al., 2017; Furlan et al., 2024), and in counterfeiting agents (e.g., security inks) (MacKenzie and Pal, 2021). The dissymmetry factor g_{lum} is used to estimate the excess of emitted right- or left-circularly polarized light in an isotropic solution. It is deduced from I_L and I_R, which represent the emission intensities of left and right circularly polarized light, respectively (Equation 1 center, Richardson, 1979; Arrico et al., 2020). This parameter is directly related to the electric dipole ($\overrightarrow{\mu_{ij}}$), the magnetic dipole ($\overrightarrow{m_{ij}}$) transition moment, and the angle between these two vectors (θ) (Equation 1 right).

$$|g_{lum}| = \frac{2 \times (I_L - I_R)}{(I_L + I_R)} = 4 \times \frac{\left(\overrightarrow{\mu_{ij}} / \overrightarrow{m_{ij}}\right) \times \cos\theta}{\left(\overrightarrow{\mu_{ij}} / \overrightarrow{m_{ij}}\right)^2 + 1}. \quad (1)$$

An important number of photons must be detected to apply chiral chromophores in CPL materials. To account for that, Zinna and coworkers introduced the CPL brightness (B_{CPL}), which combines the molar absorption extinction coefficient ($\varepsilon_{\lambda exc}$), the photoluminescence quantum yield (ϕ_{PL}), and the dissymmetry factor in Equation 2 (Arrico et al., 2020).

$$B_{CPL} = \varepsilon_{\lambda exc} \times \phi_{PL} \times |g_{lum}|/2. \quad (2)$$

Improving B_{CPL} is a current challenge as commonly bright luminescent molecules (displaying high $\varepsilon_{\lambda exc}$ and ϕ_{PL}) are usually accompanied with weak g_{lum}, as rationalized by Equation 1 because intense ED-allowed transitions (ligand-to-metal charge transfer, metal-to-ligand charge transfer, or $\pi^* \rightarrow \pi$ transitions) imply $\overrightarrow{\mu_{ij}} \gg \overrightarrow{m_{ij}}$, typically in the range of $|\overrightarrow{\mu_{ij}}|^2 \approx 75000 \cdot |\overrightarrow{m_{ij}}|^2$ (Reiné et al., 2018; Albano et al., 2020). Consequently, organic dyes and 4d/5d complexes, which display large ϕ_{PL} and $\varepsilon_{\lambda exc}$, are very challenging systems for improving the B_{CPL} due to the limiting weak g_{lum} (Saleh et al., 2014; Reiné et al., 2018; Gauthier et al., 2020; Song et al., 2022; Yoshida et al., 2024). Many strategies have been put in place to counter this limitation and to improve the dissymmetry factor, such as (i) the use of supramolecular assemblies (Sang et al., 2020) or (ii) enclosing chiral molecules into liquid crystals (Albano et al., 2020), into excimers (Nakanishi et al., 2016; Homberg et al., 2018; Hara et al., 2019; Mori, 2020), or into cyclic aromatic structures (Sato et al., 2017). The competitor to this type of molecules is lanthanide-based luminescent complexes as, thanks to the primogenic effect, the intrashell ED forbidden/MD allowed character of some emissive f-f transitions brings $|\overrightarrow{m_{ij}}|$ in the range of $|\overrightarrow{\mu_{ij}}|$, thus maximizing the dissymmetry factor (Equation 1). A large dissymmetry factor often comes with weak luminescence through direct metal center excitation (Lunkley et al., 2008; Nagata and Mori, 2020). For that purpose, intense activity in the field is dedicated to improving ϕ_{PL} and $\varepsilon_{\lambda exc}$ using approaches such as the antenna effect, which avoids the unfavorable direct excitation of the emissive metallic centers (Ward, 2010). Limited by their high cost and, more importantly, by their intrinsic kinetic lability, 4f metal ions could be difficult to handle due to the challenges of maintaining their molecular structures for applications. Chiral 3d metal ions are drawing more attention as an alternative due to their low cost and also because they benefit from the primogenic effect. However, they are limited by (i) their usual kinetic lability, (ii) the lack of efficient Laporte-forbidden d–d emissive states due to weak ligand-field strength, (iii) the mixing of the energy states with ligand-to-metal charge transfers (LMCT)/MLCT, and (iv) the important non-radiative deexcitation pathways that correspond to major handicaps. Cr^{III} complexes in octahedral geometry are exceptions because the large crystal-field stabilization energy (CFSE) found for the $3d^3$ electronic configuration (CSFE = 1.2 Δ_{oct}) makes these complexes kinetically inert (Helm and Merbach, 2005; Richens, 2005). In addition, the linear correlation of the $Cr(^4T_2)$ energy level with ligand-field splitting (LFS) limits damaging back intersystem crossing (BISC) from the low-lying excited state when strong donor atoms are bound to Cr^{3+} (Figure 1). As a result, this kind of Cr^{III} complex is known to display characteristic long-lived ED-forbidden/MD-allowed metal-centered spin-flip

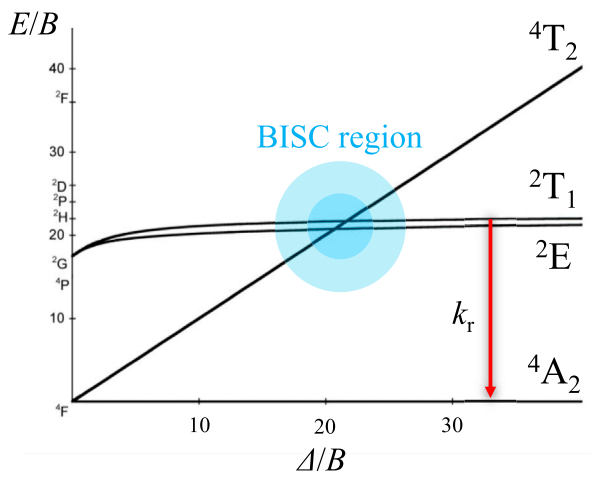

FIGURE 1
Simplified Tanabe–Sugano diagram for a d^3 electronic configuration in an octahedral field with C/B = 4.5. Two deexcitation pathways are shown: radiative (k_r, red arrow) and back intersystem crossing (BISC, blue domain). A strong LFS prevents the non-radiative deexcitation of the excited state through BISC.

$Cr(^2E \rightarrow {}^4A_2)$ and $Cr(^2T_1 \rightarrow {}^4A_2)$ NIR emission (Maiman, 1960; Kirk, 1999; Otto et al., 2015; Jimenez et al., 2019; Jiménez et al., 2020; Jimenez et al., 2021; Sinha et al., 2021).

Despite uniting the searched intrinsic kinetic inertness with emissive spin-flip transitions, the design of chiral Cr^{III} complexes with adapted absorption and emission properties remains scarce. Recently, the meridional coordination of bis-terdentate six-membered chelates rings to Cr^{III} has been demonstrated to be an interesting approach for inducing intense spin-flip chiroptical responses (Jimenez et al., 2019; Jimenez et al., 2023). In contrast, introducing chiral centers in the ligand scaffold did not lead to strong CPL emission in related complexes (Poncet et al., 2021; Cheng et al., 2023). In this context, the recent chiral resolution of the inert emissive complexes $[Cr(dqp)_2]^{3+}$ (dqp = 2,6-di(quinolin-8-yl)pyridine) (Jimenez et al., 2019) and $[Cr(ddpd)_2]^{3+}$ (ddpd = N^2,N^6-dimethyl-N^2,N^6-di(pyridin-2-yl)pyridine-2,6-diamine) (Dee et al., 2019) displaying large dissymmetry factors reactivated the interest for this topic. Concomitant high quantum yields could be obtained, making cheap and earth-abundant chromium assemblies promising candidates for CPL applications.

This work follows this strategy with the synthesis of four novel homoleptic complexes $[Cr(dqp\text{-}R)_2]^{3+}$ (R = Ph (**1**), ≡-Ph (**2**), DMA (**3**), and ≡-DMA (**4**), DMA = *N*,*N*-dimethylaniline). The photophysics of these complexes can be compared with those of the heteroleptic complexes $[Cr(dqp)(dqp\text{-}OMe)]^{3+}$ (**5**, dqp-OMe = 4-methoxy-2,6-di(quinolin-8-yl)pyridine) and $[Cr(dqp)(ddpd)]^{3+}$ (**6**) (Jimenez et al., 2020) The enantiomeric resolutions proved to be successful for all complexes, which paved the way for addressing their chiroptical properties.

2 Results and discussion

The ligands dqp-OMe, ddpd, and dqp; the salt $Cr(CF_3SO_3)_2{\cdot}2H_2O$; and the heteroleptic complexes **5** and **6** were prepared according to published methods (Supplementary

10.3389/fchem.2024.1472943

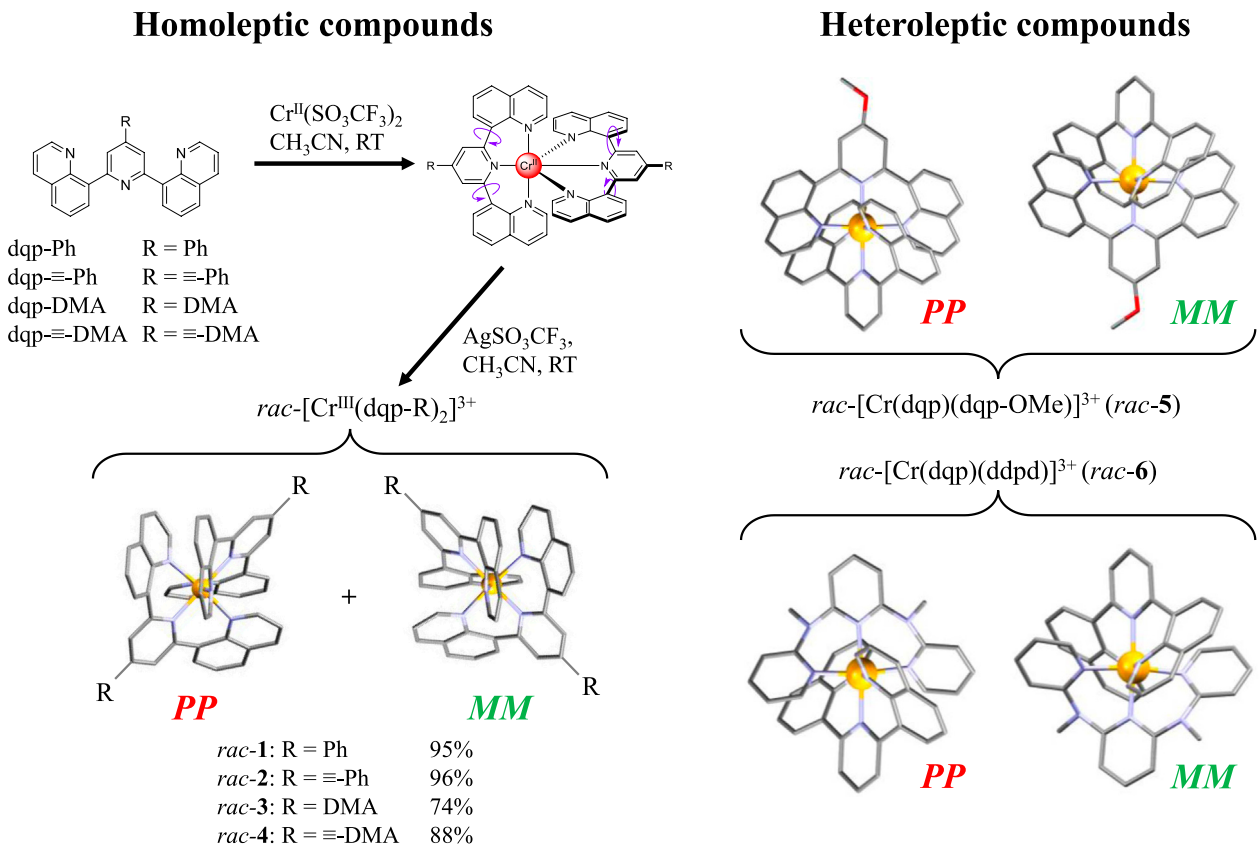

FIGURE 2
Synthesis of homoleptic complexes *rac*-$[Cr(dqp\text{-}R)_2]^{3+}$. Racemic mixtures of the *PP* and *MM* enantiomers are isolated for both homoleptic and heteroleptic complexes.

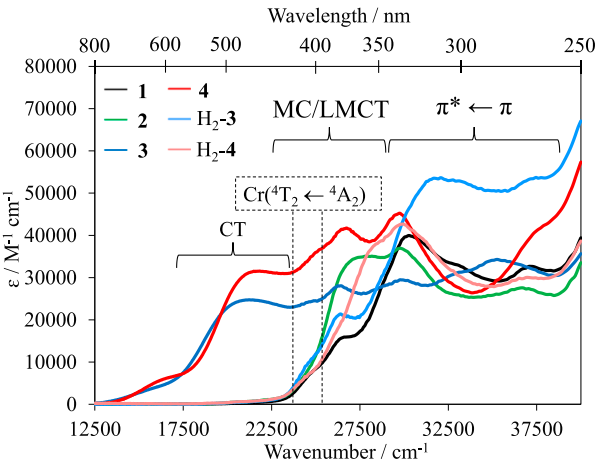

FIGURE 3
Absorption spectra of complexes **1**–**4** in H_2O and H_2-**3** and H_2-**4** in aqueous HCl (1 M) at 293 K.

Appendix 1; Cantuel et al., 2002; Otto et al., 2015; Jimenez et al., 2019; Jiménez et al., 2020). The preparation of the homoleptic complexes $[Cr(dqp\text{-}R)_2]^{3+}$ is achieved by mixing one equivalent of Cr^{II} precursor and two equivalents of the corresponding ligands dqp-R (dqp-Ph for **1**, dqp-≡-Ph for **2**, dqp-DMA for **3,** and dqp-≡-DMA for **4**) under anaerobic conditions at room temperature. The formed *rac*-$[Cr^{II}(dqp\text{-}R)_2]^{2+}$ are oxidized to the kinetically inert *rac*-$[Cr^{III}(dqp\text{-}R)_2]^{3+}$ using $AgSO_3CF_3$, affording the desired complexes in good-to-excellent yields (74%–96%, Figure 2).

Single crystals suitable for X-ray diffraction analysis (Supplementary Tables S1–S13; Supplementary Figures S1–S7 in the Supplementary Material) were obtained through slow diffusion of diethyl ether into a concentrated methanol solution for **1**, **2**, **3** (with triflate counterions), and **4** (with chlorine counterions). The dqp derivatives systematically adopt the thermodynamically more stable *meridional* binding around the kinetic labile Cr^{II} intermediate, leading to *meridional* arrangement in the final Cr^{III} complexes after oxidation. Under acidic conditions, the tertiary amine groups in **3** and **4** can be further protonated to yield $[Cr(dqp\text{-}DMAH)_2]^{5+}$ (H_2-**3**, DMAH = *N*,*N*-dimethylanilininum) and $[Cr(dqp\text{-}{\equiv}\text{-}DMAH)_2]^{5+}$ (H_2-**4**). Single crystals suitable for X-ray diffraction of both protonated complexes could also be successfully isolated by crystallization. The semi-flexible nature of the dqp backbone upon *mer* binding joined with the kinetic inertness of Cr^{III} results in the formation of racemic mixtures of helical *PP* and *MM* enantiomers of D_2-symmetry in the crystals (Figure 2). As previously reported, the two instances of intramolecular, interligand π-stacking between the aromatic quinolines produce stabilizing interactions compatible with the exclusive formation of

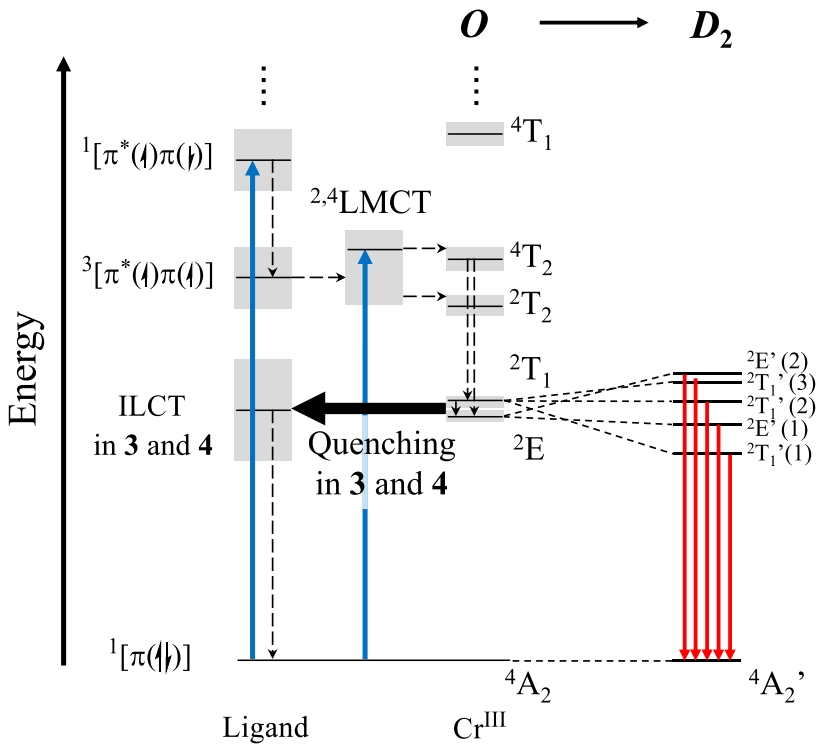

FIGURE 4
Perrin–Jablonski diagram for a Cr^{III} in *O* geometry. Excitation (blue arrows), internal conversion (dashed arrows), ILCT quenching in **3** and **4** (black arrow), and expected emission in a D_2 distorted geometry (red arrow) are represented. The splitting of the $^2T_1$ and ^2E energy levels leads to five expected optically active energy levels in D_2 symmetry.

the *PP* and *MM* enantiomers (Jimenez et al., 2021). No meso *PM* complex could be observed, likely due to steric hindrance, as simulated in the parent $[Cr(dqp)_2]^{3+}$ (Jimenez et al., 2021). To better appreciate the intramolecular interligand π-stacking, the interplanar angle is calculated as the angle between the mean plane of the 10 atoms of each quinoline (Supplementary Figures S8–S15). The closer the angle is to 0, the more parallel to each other the quinolines are. The calculated values for the complexes **1**–**5**, [H_2-**3**] and [H_2-**4**] lie within the 15.54°–16.68° range. In the heteroleptic complex $[Cr(dqp)(ddpd)]^{3+}$ (**6**), the corresponding quinoline–pyridine interplanar angle reaches 31.48°, far larger than in the other compounds, but yet smaller than the parent $[Cr(ddpd)_2]^{3+}$ (46.52°) (Otto et al., 2015). The transoid bite angles N-Cr-N are in the 176.0(1)°–177.7(8)° range for the homoleptic complexes (**1**–**4**, H_2-**3**, and H_2-**4**) and in the 175.5(9)°–176.1(10)° range for the heteroleptic complexes (**5** and **6**). In addition, to evaluate the structural distortion with respect to a perfect octahedron, the following parameter $\Sigma = \sum_{i=1}^{12}|90 - \varphi_i|$ is computed with φ_i being the cisoid bite angles N-Cr-N. The distortion in complexes **1**–**6**, H_2-**3**, and H_2-**4** ranges from $22.73° \leq \Sigma \leq 31.49°$, with the largest distortion in the heteroleptic complex **6**.

The absorption spectra of the homoleptic complexes (**1**–**4**) were recorded in water at room temperature. Complexes H_2-**3** and H_2-**4** were recorded in acidic media (aqueous HCl 1 M) to ensure full protonation of the terminal tertiary amine (Figure 3).

The maxima observed within the 345–250 nm range (29,000–40,000 cm^{-1}) are associated with $\pi^* \leftarrow \pi$ transitions located on the ligands. Ligand-to-metal charge transfers (LMCTs) are observed at lower energies from 435 nm to 345 nm (23,000–29,000 cm^{-1}). Additionally, a shoulder is observed within the 420–400 nm range (23,800–25,000 cm^{-1}), which has been assigned to the spin-allowed, parity-forbidden metal-centered (MC) $Cr(^4T_2 \leftarrow {}^4A_2)$ transition according to TD-DFT calculations performed on the parent $[Cr(dqp)_2]^{3+}$ complex (Jimenez et al., 2019). Because $\Delta = E(Cr(^4T_2 \leftarrow {}^4A_2))$ in octahedral complexes, the extracted energy values point to similar ligand-field splitting for all complexes within the 24,272–24,876 cm^{-1} range (Supplementary Table S14). Complexes **3** and **4** display an additional intense broad absorption band in the visible range of the electromagnetic spectrum 800–435 nm (12,500–23,000 cm^{-1}) assigned to the intraligand charge transfer (ILCT) from the terminal nitrogen of the aniline to the trivalent chromium center, as observed in related terpyridine-based complexes (Barbour et al., 2017). Ensuring full protonation using acidic conditions (aqueous 1 M HCl) removes the CT band in H_2-**3** and H_2-**4** (Figure 3). Moving down in energy and using an increased concentration of complexes, the spin-forbidden/parity-forbidden spin-flip (SF) transitions $Cr(^2T_1,{}^2E \leftarrow {}^4A_2)$ can be observed with low molar extinction coefficients ranging from 0.1 M^{-1} cm^{-1} to 0.6 M^{-1} cm^{-1}.

Because of the slightly distorted geometry going from O_h to D_2, a splitting of the two expected bands produces five distinct excited energy levels. The $Cr(^2T_1)$ splits into three non-degenerated energy levels, and the $Cr(^2E)$ splits into two (Figure 4; Supplementary Figures S16–S19) (Jimenez et al., 2023). Recording the SF bands was impossible in complexes **3** and **4** because of the overlap with

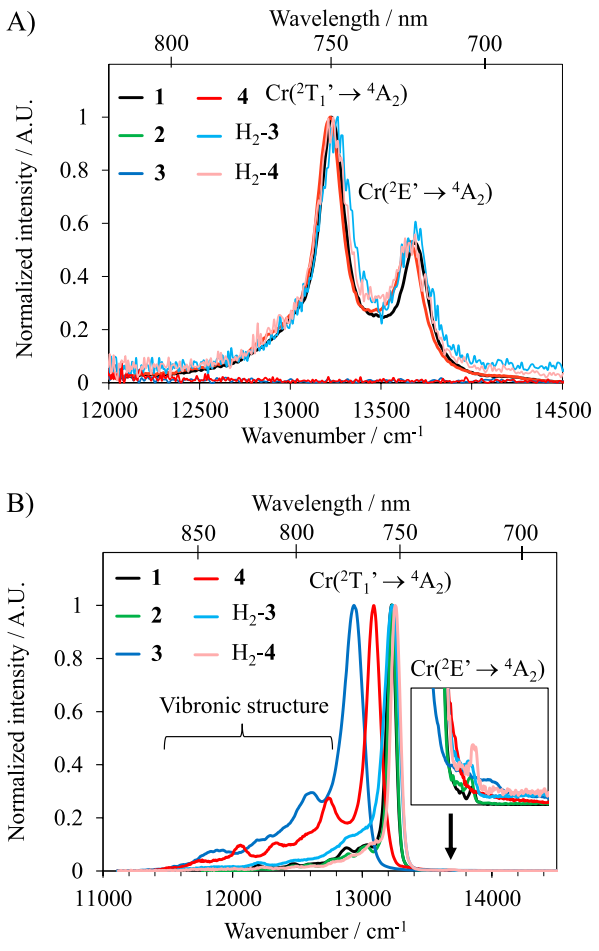

FIGURE 5
Near-infrared emission spectra with λ_{exc} = 435 nm of **(A)** Complexes **1–4** in H_2O and H_2-**3** and H_2-**4** in aqueous 1 M HCl at 293 K and **(B)** Complexes **1–4** in DMSO/H_2O 1:1 and H_2-**3** and H_2-**4** in aqueous 1 M HCl at 77 K.

the intense charge transfer absorption band in the visible region of the spectrum. Individual assignments of the absorption bands together with experimental radiative rate constants k_{rad}, radiative lifetimes τ_{rad}, oscillator strengths f_{exp}, and dipole strengths D_{exp} are compiled in Supplementary Table S14. From the absorption spectra and the calculated energies of the accessible excited levels, the ligand-field parameter Δ and the Racah parameters B and C can be estimated using Equations 3–6 (Supplementary Table S15) (Jorgensen, 1963; Witzke, 1971; Chong et al., 2022).

$$E\left({}^4T_2\right) = \Delta. \tag{3}$$

$$E\left({}^2T_1\right) = 9B + 3C - 24\left(\frac{B^2}{\Delta}\right). \tag{4}$$

$$E\left({}^2E\right) = 9B + 3C - 50\left(\frac{B^2}{\Delta}\right). \tag{5}$$

$$E\left({}^2T_2\right) = 15B + 5C - 176\left(\frac{B^2}{\Delta}\right). \tag{6}$$

$$E\left({}^4T_1\right) = 1.5\Delta + 7.5B - 0.5\sqrt{\left(225B^2 + \Delta^2 - 18\Delta B\right)}. \tag{7}$$

For all studied complexes, B ranges from 611 cm^{-1} to 655 cm^{-1}, and C ranges from 2,743 cm^{-1} to 2,885 cm^{-1}, which implies a weak impact of the extension of the π-delocalized conjugated system contrariwise to a previously reported substitution of methoxy groups in the same position in the homoleptic $[Cr(dqp\text{-}OMe)_2]^{3+}$ (Jimenez et al., 2021). We note that for the $[Cr(dqp)_2]^{3+}$, the ratio C/B equals 4.7, but the ratio is only 3.1 for $[Cr(dqp\text{-}OMe)_2]^{3+}$. Typical values are in the range of 4.2–4.9 and are sometimes assumed to be 4.7 (Adachi, 2024).

Upon UV–VIS excitation (λ_{exc} = 350–435 nm) at room temperature, the typical sharp NIR dual emissions (FWHM ≈200 cm^{-1}) observed in complexes **1** and **2** (Figure 5A) can be assigned to the radiative relaxation of the $Cr(^2E)$ and $Cr(^2T_1)$ excited state levels to the $Cr(^4A_2)$ ground state level in approximate O symmetry (Jimenez et al., 2019; Jimenez et al., 2021). The most intense band is attributed to the $Cr(^2T_1')\rightarrow{}^4A_2)$ SF transition (maxima 13,227 cm^{-1} (756 nm) in **1** and **2**) and the less intense to $Cr(^2E')\rightarrow{}^4A_2)$ (maxima at 13,698 cm^{-1} (730 nm) for **1** and 13,661 cm^{-1} (732 nm) for **2**). Contrariwise, the luminescence of complexes **3** and **4** is completely quenched, likely due to energy back transfer into the non-emissive CT levels (Figure 4). Upon protonation of the anilines (H_2-**3** and H_2-**4**), a weak luminescence is retrieved with an overall photoluminescence quantum yield of $\Phi_{PL} \leq 0.0011\%$ (Supplementary Table S16; Figure 5A), in contrast to the non-luminescent terpyridine analog (Barbour et al., 2017).

Upon changing the temperature, the Boltzmann distribution of the thermally equilibrated $Cr(^2E')$ and $Cr(^2T_1')$ levels is modified, and 77 K measurements result in a close to single emission assigned to $Cr(^2T_1')\rightarrow{}^4A_2)$ (Figure 5B). Interestingly, the total (**3** and **4**) and partial (H_2-**3** and H_2-**4**) quenching pathways of the luminescence happening at 293 K vanish at 77 K, and strong luminescence is recovered (Figure 5B). For both H_2-**3** and H_2-**4** at 77 K, the main emission band is blue-shifted compared to the non-protonated **3** and **4** complexes. The room temperature Φ_{PL} values determined in aerobic and anaerobic conditions (CH_3CN, λ_{exc} = 435 nm) are gathered in Supplementary Table S16. The obtained values in oxygen-free solutions are 12.4%, making complexes **1** and **2** in the same range as the previously reported record-holding deuterium-free Cr^{III} complexes (Jimenez et al., 2019; Jimenez et al., 2021). The origin of the high Φ_{PL} observed is attributed to (i) the weak trigonal distortion forming the octahedral geometry, preventing the non-radiative deexcitation pathways (Kitzmann et al., 2022) and (ii) the strong LFS induced by the dqp-type ligands, avoiding BISC to the $Cr(^4T_2)$ excited state level (Figure 1).

Time-resolved experiments were conducted and displayed mono-exponential decays, resulting in $\tau_{Cr,obs}^{^2E',^2T_1'} > 1$ ms in the deaerated solution at 293 K and up to 2.62(2) ms at 77 K (**2**, Supplementary Table S16; Supplementary Figures S20–S25). Air-equilibrated experiments demonstrated the extreme dependence on dissolved dioxygen, as previously reported for Cr^{III} chromophores ($\tau_{Cr,obs}^{^2E',^2T_1'} < 65$ µs) (Kirk, 1999). For more insight, the reader is referred to the in-depth analysis of the mechanism discussed by Alazaly et al. (2023).

Additionally, the rate of energy transfer from $Cr(^2E'/^2T_1')$ to O_2, k_q, can be estimated in **1** and **2** with the relationship $k_q = 1/[O_2]\cdot(1/\tau_{air} - 1/\tau_{Ar})$ (Burgin et al., 2022), in which $[O_2]$ is the oxygen concentration in the solvent at the experimental temperature

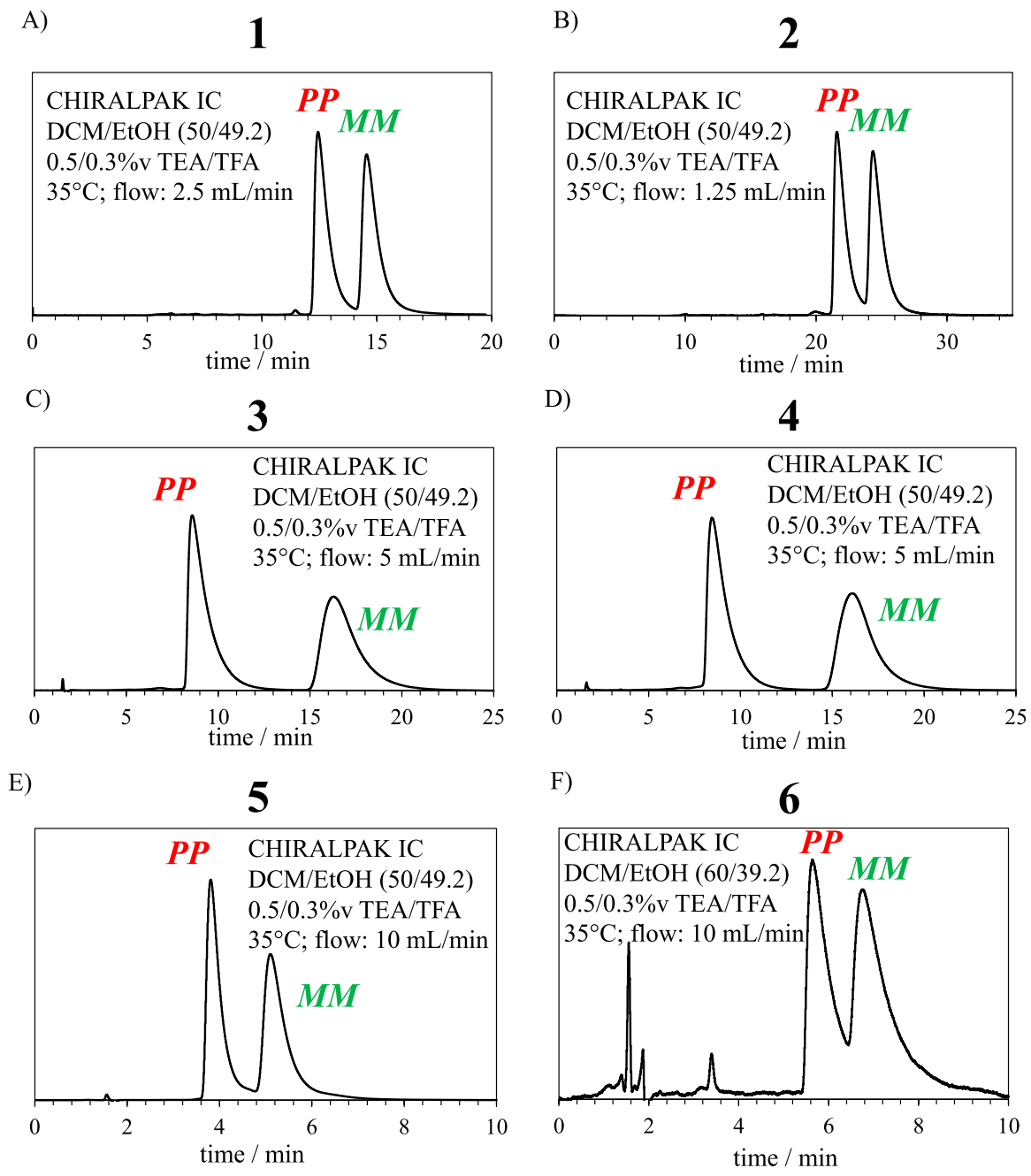

FIGURE 6
CSP-HPLC conditions required for the enantiomeric resolution of complexes **(A) 1**, **(B) 2**, **(C) 3**, **(D) 4**, **(E) 5**, and **(F) 6**.

(2.42 mM in CH_3CN at 293 K), τ_{air} is the Cr(^{2}E'/^{2}T$_1$') lifetime under air-equilibrated conditions, and τ_{Ar} is the respective lifetime under deaerated conditions. The obtained values of $6.23 \cdot 10^6$ s^{-1} (**1**) and $7.59 \cdot 10^6$ s^{-1} (**2**) demonstrate the effectiveness of O_2 quenching (Supplementary Table S16).

The thermal equilibrium of the Cr(^{2}T$_1$') and Cr(^{2}E') levels was confirmed by the recording of identical excited state lifetimes at both maxima. The sensitization efficiency for transferring the energy from the ligand to the Cr(^{2}E'/^{2}T$_1$') excited state $\eta_{sens}^{L \rightarrow Cr}$ is found to be above 71% (Supplementary Table S16). The measurement of certain photophysical properties in **3**, **4**, H_2-**3**, and H_2-**4** was limited by (i) the weak emitted signals (H_2-**3** and H_2-**4**) that prevented reliable measurements of the excited state lifetimes and (ii) the lack of emissive properties in **3** and **4**. Nevertheless, the retrieval of the luminescence at 77 K allowed time-resolved measurements on all complexes. Excitation spectra were recorded in dilute solutions and closely match the absorption spectra of the corresponding compounds (Supplementary Figures S26–S29).

Chiral stationary phase high-performance liquid chromatography (CSP-HPLC) was proven to be effective, straightforward, and quick in the separation of the racemic

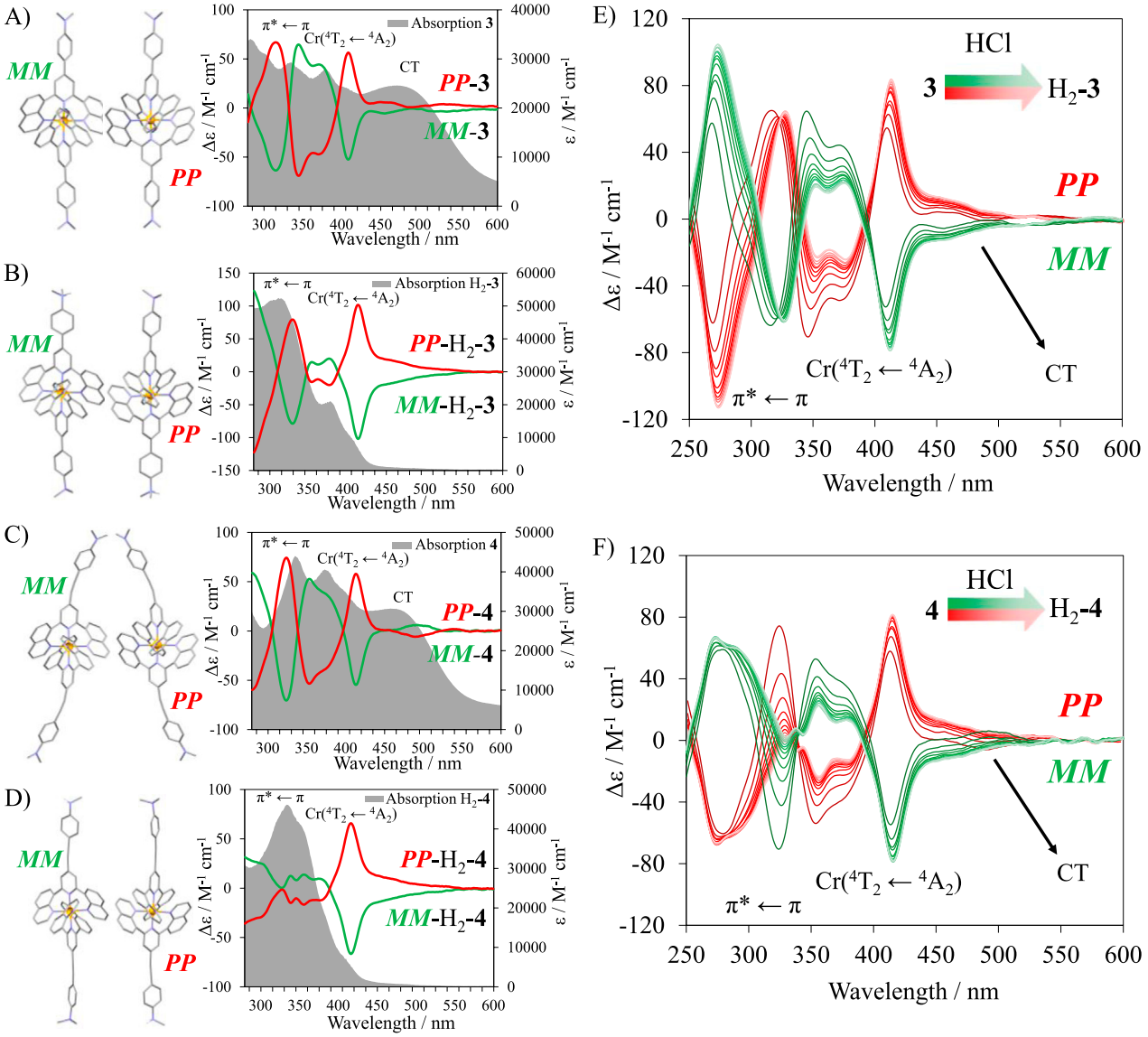

FIGURE 7
Crystalline structures of *PP* and *MM* enantiomers and the corresponding absorption (gray traces) and CD spectra (red and green traces) for **(A)** **3**, **(B)** H_2-**3**, **(C)** **4**, and **(D)** H_2-**4**. CD titration of complexes **(E)** **3** to H_2-**3** and **(F)** **4** to H_2-**4** in aqueous media.

mixture of d-block complexes such as Ru^{III}, Cr^{III}, and Co^{III} (Yoshida et al., 2013; Cortijo et al., 2017; Dee et al., 2019). Isocratic elution using a CH_2Cl_2/CH_3CH_3OH/triethylamine/trifluoroacetic acid 50/49.2/0.5/0.3 (v:v) mixture resulted in the separation of the complexes **1–6** (Figures 6A–F). For complexes **1**, **2**, and **5**, the elutions of *MM* enantiomers tail and slightly overlap with the elution peaks of the *PP* enantiomers. As a result, a small amount of contamination was observed upon reinjection in the analytical column (Supplementary Figures S30–S32). Nevertheless, thorough integrations of the chromatogram reveal that ≤0.5% mol was present in the sample. Therefore, the chiroptical studies were carried out while considering these contaminations as negligible. The obtention of a mirror image of the circular dichroism (CD) and CPL signals confirmed the adequacy of the latter assumption. Note that the efficient separation of **3** and **4** would allow a larger scale separation.

The CD was recorded, and mirror images were systematically obtained for all complexes **1–6**, H_2-**3**, and H_2-**4** (Figures 7, 8). The study of the analogous crystallized *MM*-$[Cr(dqp)_2]^{3+}$ in CD allowed the assignment of the measured complexes (Jimenez et al., 2019). In all complexes except for **6** (Figure 8D), a strong Cotton effect could be observed in the 410–430 nm range, corresponding to the MC $Cr(^4T_2 \leftarrow {}^4A_2)$ transition. The UV range is also dominated by considerable Cotton effect matching with $\pi^* \leftarrow \pi$ transitions located on the ligands. Despite the significant absorption of the CT bands in complexes **3** and **4** (ε = 25,000–32000 $M^{-1}cm^{-1}$), little to no Cotton effect was observed, confirming the low g_{abs} for these specific transitions (Figures 7A, C). Because **3** and **4** could be protonated in solution, their conversion to the respective protonated species H_2-**3** and H_2-**4** could be followed by CD upon successive addition of hydrochloric acid (0.05 M) in the aqueous solution (Figures 7E, F). The MC ligand-field

10.3389/fchem.2024.1472943

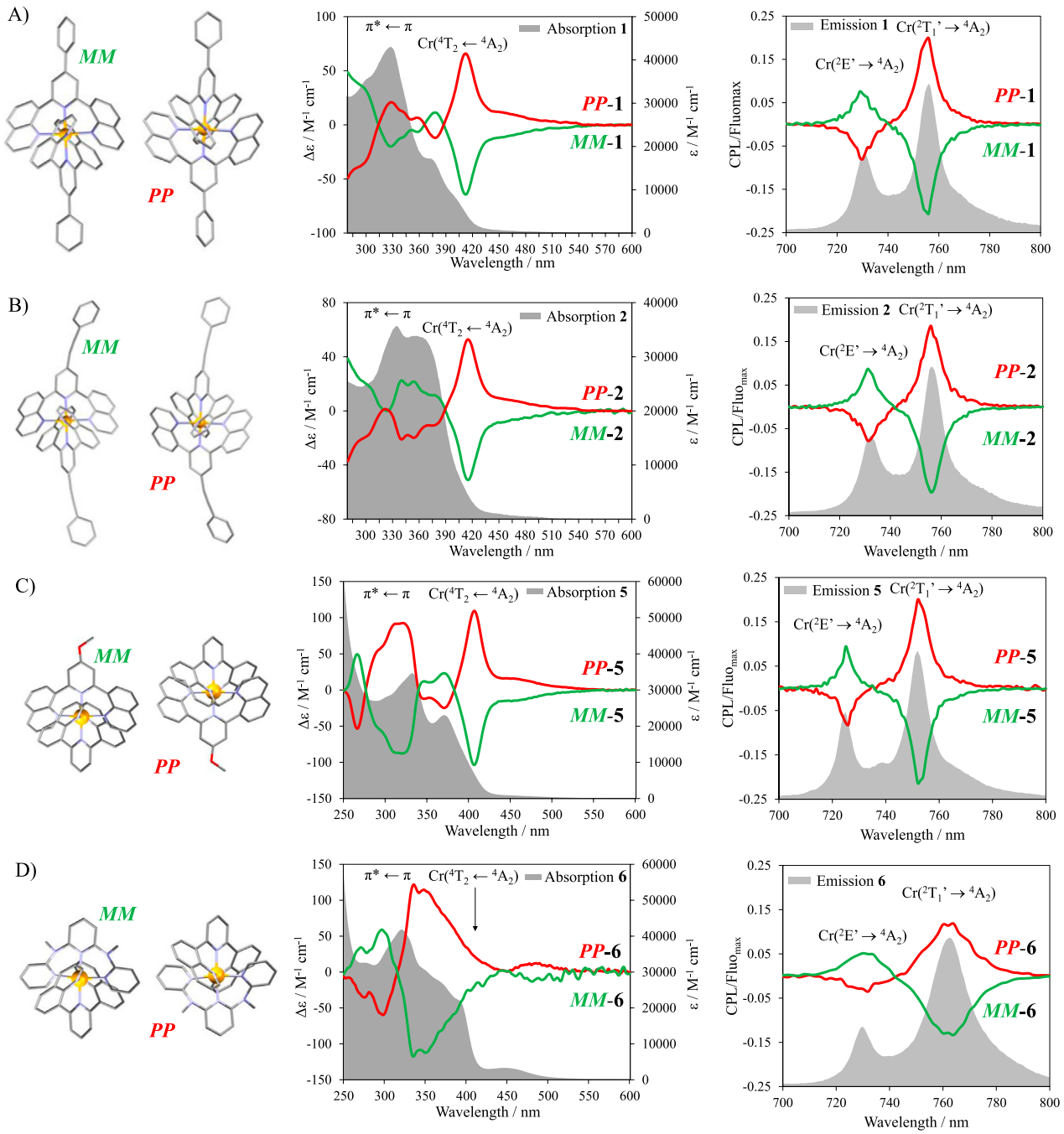

FIGURE 8
Crystalline structure of the *PP* and *MM* enantiomers and the corresponding CD (middle, red, and green traces) and CPL (λ_{exc} = 340 nm, right, (red and green traces)) spectra for **(A) 1**, **(B) 2**, **(C) 5**, and **(D) 6**. The experimental bandwidth (EBW) for the CPL spectra in A–C is 0.5 nm and 5 nm for **(D)**. The gray traces show the absorption (middle) and emission (right) spectra.

$Cr(^4T_2 \leftarrow {}^4A_2)$ transition is less affected by the protonation of the ligands than the $\pi^* \leftarrow \pi$ transitions, which display important changes in the 250–400 nm range.

Circularly polarized luminescence (CPL) measurements were recorded on each enantiomer of the emissive complexes **1**, **2**, **5**, and **6** (Figures 8A–D). The low photoluminescence quantum yield of H_2-**3** and H_2-**4** and the non-emissive character of **3** and **4** prevented CPL measurements. To ensure a correct determination of the dissymmetry factor, the highest resolution of the CPL spectra is ensured with the smallest emission slit aperture settings available at the cost of the signal intensity (Sickinger et al., 2024). The experimental bandwidth (EBW) used in these experiments is 0.5 nm for **1**, **2**, and **5** and 5 nm for **6**. A better signal-to-noise ratio can be obtained by opening the slits (larger EBW), but the resolution of the spectra must be sacrificed, skewing the results and the value of g_{lum}. It is, therefore, more correct to measure the sample at the smallest slit aperture available and divide the CPL spectra by the maximum read value of the corresponding emission.

TABLE 1 CPL brightness (B_{CPL}) calculation for each emissive transition in complexes 1, 2, 5, and 6.

Complex	ε/M^{-1}cm^{-1}	ϕ_{PL}/% [a]	$^2T_1'/^2E'$ ratio		$\lvert g_{lum}\rvert$	B_{CPL}/M^{-1}cm^{-1}
1	34,622 [b]	12.4	$^2E'$	0.324	$8{\cdot}10^{-2}$	56
			$^2T_1'$	0.676	$2{\cdot}10^{-1}$	290
2	36,118 [b]	12.4	$^2E'$	0.333	$8{\cdot}10^{-2}$	60
			$^2T_1'$	0.667	$2{\cdot}10^{-1}$	299
5	29,881 [b]	6.5	$^2E'$	0.308	$8{\cdot}10^{-2}$	24
			$^2T_1'$	0.692	$2{\cdot}10^{-1}$	134
6	32,684 [b]	6.0	$^2E'$	0.181	$7{\cdot}10^{-2}$	14
			$^2T_1'$	0.819	$1.4{\cdot}10^{-1}$	112
$[Cr(dqp)_2]^{3+}$ [c]	20,000 [d]	5.2	$^2T_1'$	-	$2{\cdot}10^{-1}$	104
$[Cr(dqp\text{-}Br)_2]^{3+}$ [e]	10,591 [f]	14	$^2T_1'$	-	$1.9{\cdot}10^{-1}$	140
$[Cr(dqp\text{-}OMe)_2]^{3+}$ [e]	5,000 [f]	17	$^2T_1'$	-	$1.8{\cdot}10^{-1}$	76.5
$[Cr(dqp\text{-}\equiv)_2]^{3+}$ [e]	13,553 [f]	15	$^2T_1'$	-	$1.7{\cdot}10^{-1}$	173
$[Cr(ddpd)_2]^{3+}$ [g]	30,000 [h]	11	$^2T_1'$	-	$9.3{\cdot}10^{-2}$	153

[a]Deaerated conditions.
[b]λ_{abs} = 340 nm.
[c]Jimemez et al., 2019.
[d]λ_{abs} = 370 nm.
[e]Jimemez et al., 2021.
[f]λ_{abs} = 405 nm.
[g]Dee et al., 2019.
[h]λ_{abs} = 300 nm.

Under unpolarized excitation (λ_{exc} = 340 nm), complexes **1**, **2**, **5**, and **6** (Figures 8A–D) displayed strong circularly polarized emission within the 720–780 nm range. The dissymmetry factors $\lvert g_{lum}\rvert$ obtained for the Cr($^2E'\rightarrow{}^4A_2$) transition reach 0.07–0.08 for all four complexes (Supplementary Figures S33–S36). Interestingly, for the Cr($^2T_1'\rightarrow{}^4A_2$) transition, complexes **1**, **2**, and **5** display $\lvert g_{lum}\rvert$ = 0.20, whereas complex **6** reaches only $\lvert g_{lum}\rvert$ = 0.14.

Putting these results in perspective with those of the previously reported homoleptic complexes of $[Cr(ddpd)_2]^{3+}$ and $[Cr(dqp\text{-}R)_2]^{3+}$ (R = H, Br, OMe, C≡CH, Table 1) (Otto et al., 2015; Jimenez et al., 2019; Jimenez et al., 2021), a trend emerges for the Cr($^2T_1'\rightarrow{}^4A_2$) transitions. Indeed, all complexes containing two dqp-based ligands display the same dissymmetry factor of 0.2, whereas the more flexible $[Cr(ddpd)_2]^{3+}$ culminated at 0.093 (Dee et al., 2019). By exploiting the chemical inertness of Cr^{III}, one of each ligand could be implemented in the same complex to give the heteroleptic complex $[Cr(dqp)(ddpd)]^{3+}$ (**6**), for which $\lvert g_{lum}\rvert$ = 0.14 corresponds to the average of the dissymmetry factors of the two parent homoleptic complexes. As an attempt to rationalize this result, a hypothetical "ligand dissymmetry factor" g_{lum}^{L} could be imagined for a given transition defined as Equation 8.

$$\left|g_{lum}^{L}\right| = \frac{\eta^{L}}{n} \cdot \left|g_{lum}^{total,homoleptic}\right|. \quad (8)$$

η^L is the denticity of the ligand, n the number of available coordination sites around the metal center (6 for octahedral symmetry), and $g_{lum}^{total,homoleptic}$ is the dissymmetry factor of the corresponding homoleptic complex of a specific transition. Therefore, in the cases of $[Cr(dqp)_2]^{3+}$ and $[Cr(ddpd)_2]^{3+}$, the following values are obtained: $g_{lum}^{dqp} = 0.1$ and $g_{lum}^{ddpd} = 0.0465$. From these values, the dissymmetry factor of a heteroleptic complex could be estimated by applying Equation 9.

$$\left|g_{lum}^{total,heteroleptic}\right| = \sum \left|g_{lum}^{L}\right|. \quad (9)$$

For **2**, one obtains $g_{lum}^{dqp} + g_{lum}^{ddpd} = 0.1 + 0.0465 = 0.1465$, which corresponds closely to the experimental value of 0.14, verifying the hypothesis. Unfortunately, the number of available compounds is limited; thus, to validate or invalidate the statement, more flexible tridentate ligands must be studied. As a general conclusion to the chiroptic luminescence, an extension of the organic π-delocalized electronic cloud in the *para* position of the pyridine does not influence the dissymmetry factor, while the implementation of ddpd ligands results in an attenuated g_{lum}. A plausible explanation for this observation is that the rigidification of the complex is key in the obtention of a large dissymmetry factor, and the rigidity must be maximized.

The B_{CPL} of the emissive complexes can be calculated using Equation 2. Because the g_{lum} values associated with the two observed emissions Cr($^2T_1'\rightarrow{}^4A_2$) and Cr($^2E'\rightarrow{}^4A_2$) are of opposite signs in the same enantiomer, B_{CPL} must be similarly split into two components. Accordingly, the ϕ_{PL} must be split relative to the intensity of each band at the temperature measurement (293 K). The emission spectrum of the corresponding complex is approximated as two Gaussian curves, deconvoluted as such, and the ratio between them is calculated (idealized Cr($^2T_1\rightarrow{}^4A_2$) and

$Cr(^2E \rightarrow {}^4A_2)$ transitions, Supplementary Figures S37–S40). The calculated values of B_{CPL} are compiled in Table 1 and range from 299 $M^{-1}cm^{-1}$ to 122 $M^{-1}cm^{-1}$ for the $Cr(^2T_1' \rightarrow {}^4A_2)$ transition and 60–14 $M^{-1}cm^{-1}$ for the $Cr(^2E' \rightarrow {}^4A_2)$ transition, which are among the highest reported values for CPL active compounds (Arrico et al., 2020). A higher B_{CPL} can be achieved by exciting the maxima of the absorption band to increase the value of ε in the B_{CPL} calculation. The ϕ_{PL} is considered invariant with the excitation wavelength.

3 Conclusion

A series of new chiral homoleptic and heteroleptic Cr^{III} chromophores with dqp-based ligands with *para* functionalization of the central pyridine have been synthesized and characterized. The addition of *N*,*N*-dimethylaniline to the complex resulted in a large increase in absorbance in the VIS region (CT) accompanied by quenching of the luminescence. Interestingly, weak luminescence is retrieved upon protonation of the aniline ($\Phi_{PL} \leq 0.0011\%$). The highly luminescent complexes $[Cr(dqp\text{-}Ph)_2]^{3+}$ and $[Cr(dqp\text{-}{\equiv}\text{-}Ph)_2]^{3+}$ are promising candidates for use as chiral luminescent probes. Enantiomeric resolution of all six racemic complexes could be achieved by CSP-HPLC. Implementing *N*,*N*-dimethylaniline as a substituent to the complex resulted in a baseline separation of the two enantiomers, allowing a potential large-scale separation. Moreover, the evolution of the circular dichroism from the non-protonated to the protonated species in $[Cr(dqp\text{-}DMA)_2]^{3+}$/$[Cr(dqp\text{-}DMAH)_2]^{5+}$ and $[Cr(dqp\text{-}{\equiv}\text{-}DMA)_2]^{3+}$/$[Cr(dqp\text{-}{\equiv}\text{-}DMAH)_2]^{5+}$ could be followed. Near-perfect octahedral geometries are obtained with the help of the six-membered chelate rings, providing long excited state lifetime and high overall photoluminescence quantum yields at room temperature. Dual circularly polarized luminescence arises from the $Cr(^2T_1')$ and $Cr(^2E')$ excited level to the $Cr(^4A_2)$ ground state within the 720–780 nm range. The observed $|g_{lum}|$ for the emissive complexes amounts to 0.2 except for $[Cr(dqp)(ddpd)]^{3+}$, for which the $|g_{lum}|$ was measured to be in between the two corresponding parent homoleptic complexes $[Cr(dqp)_2]^{3+}$ ($|g_{lum}| = 0.2$) and $[Cr(ddpd)_2]^{3+}$ ($|g_{lum}| = 0.093$). High B_{CPL} values, ranging from 299 $^{-1}cm^{-1}$ to 122 $M^{-1}cm^{-1}$ for the $Cr(^2T_1' \rightarrow {}^4A_2)$ transition and 60–14 $M^{-1}cm^{-1}$ for the $Cr(^2E' \rightarrow {}^4A_2)$ transition, were obtained, reaching the typical range of 4f-based chiral chromophores with the added value of the inertness and low cost of trivalent chromium.

Data availability statement

The original contributions presented in the study are included in the article/Supplementary Material, further inquiries can be directed to the corresponding authors.

Author contributions

MP: conceptualization, formal analysis, investigation, and writing–original draft. CB: formal analysis and writing–review and editing. LG: formal analysis and writing–review and editing. J-RJ: conceptualization, supervision, validation, and writing–review and editing. CP: conceptualization, funding acquisition, supervision, validation, and writing–review and editing.

Funding

The author(s) declare that financial support was received for the research, authorship, and/or publication of this article. This work is supported through grants from the Swiss National Science Foundation (grant 200020_207313). Financial support from the Swiss National Science Foundation is gratefully acknowledged. J-RJ acknowledges the funding received from the grant TED2021.129598A.I00 funded by MCIN/AEI/10.13039/501100011033 and by European Union NextGenerationEU/PRTR and is grateful to the Ministerio de Ciencia Innovación y Universidades for a Ramón y Cajal contract (grant RYC 2022-037255-I) funded by MCIN/AEI/10.13039/501100011033 and FSE+.

Acknowledgments

K. L. Buchwalder is acknowledged for performing elemental analysis.

Conflict of interest

The authors declare that the research was conducted in the absence of any commercial or financial relationships that could be construed as a potential conflict of interest.

Publisher's note

Supplementary material

The Supplementary Material for this article can be found online at: https://www.frontiersin.org/articles/10.3389/fchem.2024.1472943/full#supplementary-material

References

Adachi, S. (2024). Practical consideration on Racah parameter and Tanabe–Sugano diagram analyses for Mn4+ and Cr3+-activated phosphors. *J. Luminescence* 273, 120628. doi:10.1016/j.jlumin.2024.120628

Alazaly, A. M. M., Clarkson, G. J., Ward, M. D., and Abdel-Shafi, A. A. (2023). Mechanism of oxygen quenching of the excited states of heteroleptic chromium(III) phenanthroline derivatives. *Inorg. Chem.* 62, 16101–16113. doi:10.1021/acs.inorgchem.3c02343

Albano, G., Pescitelli, G., and Di Bari, L. (2020). Chiroptical properties in thin films of π-conjugated systems. *Chem. Rev.* 120, 10145–10243. doi:10.1021/acs.chemrev.0c00195

Arrico, L., Di Bari, L., and Zinna, F. (2020). Quantifying the overall efficiency of circularly polarized emitters. *Chem. – A Eur. J.* 27, 2920–2934. doi:10.1002/chem.202002791

Barbour, J. C., Kim, A. J. I., deVries, E., Shaner, S. E., and Lovaasen, B. M. (2017). Chromium(III) bis-arylterpyridyl complexes with enhanced visible absorption via incorporation of intraligand charge-transfer transitions. *Inorg. Chem.* 56, 8212–8222. doi:10.1021/acs.inorgchem.7b00953

Brandt, J. R., Salerno, F., and Fuchter, M. J. (2017). The added value of small-molecule chirality in technological applications. *Nat. Rev. Chem.* 1, 0045. doi:10.1038/s41570-017-0045

Burgin, T. H., Glaser, F., and Wenger, O. S. (2022). Shedding light on the oxidizing properties of spin-flip excited states in a Cr(III) polypyridine complex and their use in photoredox catalysis. *J. Am. Chem. Soc.* 144, 14181–14194. doi:10.1021/jacs.2c04465

Cantuel, M., Bernardinelli, G., Imbert, D., Bünzli, J.-C. G., Hopfgartner, G., and Piguet, C. (2002). A kinetically inert and optically active Cr(III) partner in thermodynamically self-assembled heterodimetallic non-covalent d-f podates. *J. Chem. Soc. Dalton Trans.*, 1929–1940. doi:10.1039/B200011C

Carr, R., Evans, N. H., and Parker, D. (2012). Lanthanide complexes as chiral probes exploiting circularly polarized luminescence. *Chem. Soc. Rev.* 41, 7673–7686. doi:10.1039/C2CS35242G

Cheng, Y., He, J., Zou, W., Chang, X., yang, Q., and Lu, W. (2023). Circularly polarized near-infrared phosphorescence of chiral chromium(III) complexes. *Chem. Commun.* 59, 1781–1784. doi:10.1039/D2CC06548G

Chong, J., Besnard, C., Cruz, C. M., Piguet, C., and Jimenez, J. R. (2022). Heteroleptic mer-[Cr(NNN)(CN)3] complexes: synthetic challenge, structural characterization and photophysical properties. *Dalton Trans.* 51, 4297–4309. doi:10.1039/d2dt00126h

Cortijo, M., Viala, C., Reynaldo, T., Favereau, L., Fabing, I., Srebro-Hooper, M., et al. (2017). Synthesis, spectroelectrochemical behavior, and chiroptical switching of tris(β-diketonato) complexes of ruthenium(III), chromium(III), and cobalt(III). *Inorg. Chem.* 56, 4555–4567. doi:10.1021/acs.inorgchem.6b03094

Dee, C., Zinna, F., Kitzmann, W. R., Pescitelli, G., Heinze, K., Di Bari, L., et al. (2019). Strong circularly polarized luminescence of an octahedral chromium(III) complex. *Chem. Comm.* 55, 13078–13081. doi:10.1039/c9cc06909g

Furlan, F., Moreno-Naranjo, J. M., Gasparini, N., Feldmann, S., Wade, J., and Fuchter, M. J. (2024). Chiral materials and mechanisms for circularly polarized light-emitting diodes. *Nat. Photonics* 18, 658–668. doi:10.1038/s41566-024-01408-z

Gauthier, E. S., Abella, L., Hellou, N., Darquié, B., Caytan, E., Roisnel, T., et al. (2020). Long-lived circularly polarized phosphorescence in helicene-NHC rhenium(I) complexes: the influence of helicene, halogen, and stereochemistry on emission properties. *Angew. Chem. Int. Ed.* 59, 8394–8400. doi:10.1002/anie.202002387

Hara, N., Okuda, K., Shizuma, M., Tajima, N., and Imai, Y. (2019). Control of circularly polarised luminescence using a suitable wired structure connecting a binaphthyl with two pyrenes. *ChemistrySelect* 4, 10209–10213. doi:10.1002/slct.201902176

Heffern, M. C., Matosziuk, L. M., and Meade, T. J. (2014). Lanthanide probes for bioresponsive imaging. *Chem. Rev.* 114, 4496–4539. doi:10.1021/cr400477t

Helm, L., and Merbach, A. E. (2005). Inorganic and bioinorganic solvent exchange mechanisms. *Chem. Rev.* 105, 1923–1960. doi:10.1021/cr030726o

Homberg, A., Brun, E., Zinna, F., Pascal, S., Górecki, M., Monnier, L., et al. (2018). Combined reversible switching of ECD and quenching of CPL with chiral fluorescent macrocycles. *Chem. Sci.* 9, 7043–7052. doi:10.1039/C8SC02935K

Jimenez, J. R., Doistau, B., Cruz, C. M., Besnard, C., Cuerva, J. M., Campana, A. G., et al. (2019). Chiral molecular ruby [Cr(dqp)2](3+) with long-lived circularly polarized luminescence. *J. Am. Chem. Soc.* 141, 13244–13252. doi:10.1021/jacs.9b06524

Jimenez, J. R., Miguez-Lago, S., Poncet, M., Ye, Y. T., Ruiz, C. L., Cruz, C. M., et al. (2023). Eu-III functionalized silica nanoparticles encapsulating chiral Cr-III complexes with simultaneous unpolarized red and polarized NIR-I luminescence. *J. Mater. Chem. C* 11, 2582–2590. doi:10.1039/d2tc05344f

Jiménez, J.-R., Poncet, M., Doistau, B., Besnard, C., and Piguet, C. (2020). Luminescent polypyridyl heteroleptic CrIII complexes with high quantum yields and long excited state lifetimes. *Dalton Trans.* 49, 13528–13532. doi:10.1039/D0DT02872J

Jimenez, J. R., Poncet, M., Miguez-Lago, S., Grass, S., Lacour, J., Besnard, C., et al. (2021). Bright long-lived circularly polarized luminescence in chiral chromium(III) complexes. *Angew. Chem. Int. Ed.* 60, 10095–10102. doi:10.1002/anie.202101158

Jorgensen, C. K. (1963). Spectroscopy of transition-group complexes. *Adv. Chem. Phys.* 5, 33–146. doi:10.1002/9780470143513.ch2

Kirk, A. D. (1999). Photochemistry and photophysics of chromium(III) complexes. *Chem. Rev.* 99, 1607–1640. doi:10.1021/cr960111+

Kitzmann, W. R., Ramanan, C., Naumann, R., and Heinze, K. (2022). Molecular ruby: exploring the excited state landscape. *Dalton Trans.* 51, 6519–6525. doi:10.1039/d2dt00569g

Lunkley, J. L., Shirotani, D., Yamanari, K., Kaizaki, S., and Muller, G. (2008). Extraordinary circularly polarized luminescence activity exhibited by cesium tetrakis(3-heptafluoro-butylryl-(+)-camphorato) Eu(III) complexes in EtOH and CHCl3 solutions. *J. Am. Chem. Soc.* 130, 13814–13815. doi:10.1021/ja805681w

MacKenzie, L. E., and Pal, R. (2021). Circularly polarized lanthanide luminescence for advanced security inks. *Nat. Rev. Chem.* 5, 109–124. doi:10.1038/s41570-020-00235-4

Maiman, T. H. (1960). Stimulated optical radiation in ruby. *Nature* 187, 493–494. doi:10.1038/187493a0

Mori, T. (2020). *Circularly polarized luminescence of isolated small organic molecules*. Singapore: Springer. doi:10.1007/978-981-15-2309-0

Nagata, Y., and Mori, T. (2020). Irreverent nature of dissymmetry factor and quantum yield in circularly polarized luminescence of small organic molecules. *Front. Chem.* 8, 448. doi:10.3389/fchem.2020.00448

Nakanishi, S., Nakabayashi, K., Mizusawa, T., Suzuki, N., Guo, S., Fujiki, M., et al. (2016). Cryptochiral binaphthyl–bipyrene luminophores linked with alkylene esters: intense circularly polarised luminescence, but ultraweak circular dichroism. *RSC Adv.* 6, 99172–99176. doi:10.1039/C6RA20342F

Otto, S., Grabolle, M., Förtser, C., Kreitner, C., Resh-Genger, U., and Heinze, K. (2015). [Cr(ddpd)2]3+: a molecular, water-soluble, highly NIR-emisssive Ruby analogue. *Angew. Chem. Int. Ed.* 54, 11572–11576. doi:10.1002/anie.201504894

Poncet, M., Benchohra, A., Jimenez, J. R., and Piguet, C. (2021). Chiral chromium(III) complexes as promising candidates for circularly polarized luminescence. *Chemphotochem* 5, 880–892. doi:10.1002/cptc.202100146

Reiné, P., Justicia, J., Morcillo, S. P., Abbate, S., Vaz, B., Ribagorda, M., et al. (2018). Pyrene-containing ortho-Oligo(phenylene)ethynylene foldamer as a ratiometric probe based on circularly polarized luminescence. *J. Org. Chem.* 83, 4455–4463. doi:10.1021/acs.joc.8b00162

Richardson, F. S. (1979). Theory of optical activity in the ligand-field transitions of chiral transition metal complexes. *Chem. Rev.* 79, 17–42. doi:10.1021/cr60317a003

Richens, D. T. (2005). Ligand substitution reactions at inorganic centers. *Chem. Rev.* 105, 1961–2002. doi:10.1021/cr030705u

Saleh, N., Shen, C., and Crassous, J. (2014). Helicene-based transition metal complexes: synthesis, properties and applications. *Chem. Sci.* 5, 3680–3694. doi:10.1039/C4SC01404A

Sang, Y., Han, J., Zhao, T., Duan, P., and Liu, M. (2020). Circularly polarized luminescence in nanoassemblies: generation, amplification, and application. *Adv. Mater.* 32, 1900110. doi:10.1002/adma.201900110

Sato, S., Yoshii, A., Takahashi, S., Furumi, S., Takeuchi, M., and Isobe, H. (2017). Chiral intertwined spirals and magnetic transition dipole moments dictated by cylinder helicity. *Proc. Natl. Acad. Sci.* 114, 13097–13101. doi:10.1073/pnas.1717524114

Sickinger, A., Baguenard, B., Bensalah-Ledoux, A., Guyot, Y., Guy, L., Pointillart, F., et al. (2024). Impact of the experimental bandwidth on circularly polarized luminescence measurements of lanthanide complexes: the case of erbium(iii). *J. Mater. Chem. C* 12, 4253–4260. doi:10.1039/D3TC04717B

Sinha, N., Jimenez, J. R., Pfund, B., Prescimone, A., Piguet, C., and Wenger, O. S. (2021). A near-infrared-II emissive chromium(III) complex. *Angew. Chem. Int. Ed.* 60, 23722–23728. doi:10.1002/anie.202106398

Song, J., Xiao, H., Fang, L., Qu, L., Zhou, X., Xu, Z.-X., et al. (2022). Highly phosphorescent planar chirality by bridging two square-planar platinum(II) complexes: chirality induction and circularly polarized luminescence. *J. Am. Chem. Soc.* 144, 2233–2244. doi:10.1021/jacs.1c11699

Staszak, K., Wieszczycka, K., Marturano, V., and Tylkowski, B. (2019). Lanthanides complexes – chiral sensing of biomolecules. *Coord. Chem. Rev.* 397, 76–90. doi:10.1016/j.ccr.2019.06.017

Ward, M. D. (2010). Mechanisms of sensitization of lanthanide(III)-based luminescence in transition metal/lanthanide and anthracene/lanthanide dyads. *Coord. Chem. Rev.* 254, 2634–2642. doi:10.1016/j.ccr.2009.12.001

Witzke, H. (1971). Semi-empirical evaluations of the Racah B and C parameters from the crystal field spectra of chromium(III) complexes. *Theor. Chim. Acta* 20, 171–185. doi:10.1007/BF00569263

Yoshida, J., Watanabe, G., Kakizawa, K., Kawabata, Y., and Yuge, H. (2013). Tris(β-diketonato) Ru(III) complexes as chiral dopants for nematic liquid crystals: the effect of the molecular structure on the helical twisting power. *Inorg. Chem.* 52, 11042–11050. doi:10.1021/ic401240f

Yoshida, K., Kajiwara, M., Okazaki, Y., Véronique, L., Zinna, F., Sojic, N., et al. (2024). Modulation of circularly polarized luminescence by swelling of microgels functionalized with enantiopure [Ru(bpy)3]2+ luminophores. *Chem. Commun.* 60, 1743–1746. doi:10.1039/D3CC04391F

Zinna, F., Pasini, M., Galeotti, F., Botta, C., Di Bari, L., and Giovanella, U. (2017). Design of lanthanide-based OLEDs with remarkable circularly polarized electroluminescence. *Adv. Funct. Mater.* 27, 1603719. doi:10.1002/adfm.201603719